Nuclear Science and Techniques (2026) 37:97
https://doi.org/10.1007/s41365-026-01913-6

Investigation of dynamic seismic response in liquid-containing structures for nuclear reactors using the hybrid Eulerian–Lagrangian method

Shi-Lin Chen[1,2] · Qing-Xi Yang[1] · Qing-Zhou Yu[1,2] · Hao Xu[1] · Jian Chen[1] · Zhao-Xi Chen[1]

Received: 2 August 2024 / Revised: 26 October 2024 / Accepted: 31 October 2024 / Published online: 21 March 2026

Abstract
Liquid-containing structures, including steam generators, water-cooling systems, in-containment refueling water storage tanks, suppression tanks, and tritiated water storage facilities, are integral components of nuclear reactor systems and are crucial for ensuring operational safety and stability. Traditional seismic analysis methods often struggle to accurately predict the dynamic behavior of such structures, particularly under transient events such as earthquakes. This paper presents a comprehensive study that applies the hybrid Eulerian–Lagrangian method to analyze fluid–structure interactions within these structures. The efficacy of this method for capturing the complex dynamics induced by liquid movement is demonstrated through simulations conducted primarily in a vertical storage tank. A comparative analysis with traditional response-spectrum analysis methods underscores the limitations of conventional approaches, particularly in terms of accounting for nonlinear free-surface motions and dynamic velocity distributions. The structural response of the tank containing liquid calculated using the hybrid Eulerian–Lagrangian method is approximately twice that calculated using the response-spectrum method, whereas in the case of a tank without liquid, the response is the same. Additionally, a high dynamic stress distribution exists near the liquid level of the structure. This study addresses the intricate interplay between structural components and fluid dynamics, thereby extrapolating insights from tanks to enhance safety protocols and design considerations for future nuclear devices.

Keywords Liquid-containing structures · Nuclear reactors · Seismic analysis methods · Hybrid Euler–Lagrangian method · Complex dynamics

1 Introduction

As the global demand for sustainable and clean energy escalates amidst ongoing environmental and resource challenges, nuclear energy emerges as a pivotal technology capable of transforming the energy landscape. Facilities such as Generation IV nuclear reactors [1, 2], international thermonuclear experimental reactors [3], and Chinese fusion engineering testing reactors [4] exemplify the cutting-edge advancements in harnessing nuclear power. Given the critical importance of these technologies, ensuring the operational safety and stability of nuclear reactors is of paramount importance. A crucial aspect of safety is a comprehensive seismic analysis of liquid-containing structures, as detailed in Table 1 [5–12].

One of the primary concerns in the seismic analysis of liquid-containing structures is the phenomenon of sloshing, which can significantly affect the dynamic response of a system [13, 14]. Sloshing refers to the movement of liquid in partially filled containers and can lead to substantial hydrodynamic loads on a structure, potentially compromising its integrity during seismic events. Probabilistic assessment methods based on numerical simulations can more accurately predict sloshing behavior while considering uncertainties in ground motion characteristics and tank geometry [15, 16]. Energy dissipation systems, such

This work was supported by the Fusion Vacuum Electrophysics Device Design and Development Project (No. Y15HX11706).

✉ Zhao-Xi Chen
chenzx@ipp.ac.cn

1 Hefei Institutes of Physical Science, Chinese Academy of Sciences, Hefei 230031, China

2 University of Science and Technology of China, Hefei 230026, China

Table 1 Liquid-containing structures in nuclear reactors

Reactor	Accessory system	Specific components	Internal fluids
Fission reactor	Reactor pressure vessel [5]	Vessel	Moderator
			Coolant
	Cooling system [6]	Steam Generator	Water
	In-containment refueling water storage tank system [7]	Storage tanks	Water
	Circulating water system [8]	Cooling towers	Water
Fusion reactor	Liquid plant in cryoplant [9]	Cold boxes	Liquid He
		Compressors	Liquid N_2
		Tanks	
	Cooling water systems [10]	Cooling towers	Water
		Basins	
	Vacuum vessel pressure suppression system [11]	Large leak tanks	Water
		Small leak tanks	
	Tritiated water storage area [12]	Drain tanks	Water
		Collection tanks	

as damped floating roofs, have proven to be effective in mitigating sloshing effects in steel tanks under earthquake loading [17, 18]. Comprehensive studies have emphasized the need for advanced numerical methods to capture nonlinear effects and fluid–structure coupling in sloshing dynamics [19]. These investigations underscore the limitations of simplified analytical models and highlight the importance of three-dimensional analysis, particularly for nuclear reactor applications, in which safety margins are critical.

However, traditional seismic analysis methods often fail to accurately predict the dynamic behavior of these structures during transient events such as earthquakes, primarily because of their limited ability to account for complex fluid–structure interactions (FSI) [20–25]. Considerable research has been conducted to better understand the interactions between seismic events and liquid-containing structures and to demonstrate the significance of these interactions for structural safety and integrity [26–29]. Despite these advancements, the current methodologies often lack precision in fully capturing the spectra of fluid dynamics and structural responses.

To address FSI problems involving liquid storage tanks, which involve complex interactions between fluids and solid structures under various loading conditions, recent advancements have facilitated the development of numerous sophisticated numerical methods. These methods can be broadly categorized into particle, grid, and finite-element methods, each offering unique advantages in modeling FSI. Particle-based methods offer a Lagrangian perspective on fluid and particle dynamics. Smoothed particle hydrodynamics (SPH) is used for fluid dynamics simulations and provides significant flexibility by eliminating the need for a mesh. This is particularly advantageous for simulations involving extreme deformations [30–32]. However, the SPH can suffer from stability and accuracy issues if not carefully implemented. The discrete element method (DEM), which is primarily used for granular materials rather than fluids, can be combined with fluid dynamics simulations in hybrid approaches such as CFD-DEM for fluid-particle interactions [33–35]. Grid-based methods, such as the immersed boundary method (IBM) and the Lattice Boltzmann Method (LBM), offer alternative approaches. The IBM employs a Eulerian description for fluids combined with a Lagrangian framework for structures, avoiding the need for body-fitted meshes and simplifying simulations involving complex geometries and large deformations [36–38]. The LBM provides a mesoscopic approach to fluid dynamics simulations, excelling at handling flows with complex boundary conditions and intricate geometries, owing to its parallel-processing capabilities [39–41]. Finite-element methods include the arbitrary Lagrangian–Eulerian (ALE) and coupled Eulerian–Lagrangian (CEL) methods. The ALE method addresses problems in which large mesh distortions occur by allowing the mesh to move and deform independently of its material [42–44]. Although this is effective for large deformations, its setup and computation can be intricate and time-consuming. The CEL method combines the strengths of both descriptions, providing robust solutions for dynamic material interactions, although it requires extensive computational resources to accurately resolve phase interfaces [45–47]. A notable variant of the finite-element framework is the spectral finite-element method (SFEM), which combines spectral accuracy with finite-element flexibility to achieve exponential convergence for smoothing problems [48–50]. Table 2 summarizes the various methods used in fluid–structure interaction analysis, highlighting their unique features and typical applications.

In this context, the hybrid Eulerian–Lagrangian (HEL) method represents a significant advancement in FSI analysis of nuclear reactor systems. The HEL method merges the robustness of the CEL method with the flexibility of the ALE method, enhancing the simulation accuracy by dynamically adapting the mesh based on the physical demands of the scenario. This method addresses complex challenges such as nonlinear free-surface motions and dynamic velocity distributions, which are often inadequately captured by traditional response-spectrum analysis. A comparative illustration shown in Fig. 1 highlights the superiority of this approach over conventional methods and demonstrates its capability to capture the critical dynamics essential for the safety and stability of nuclear reactors. This comprehensive approach improves the understanding of seismic behaviors in liquid-containing structures, bolsters design and safety

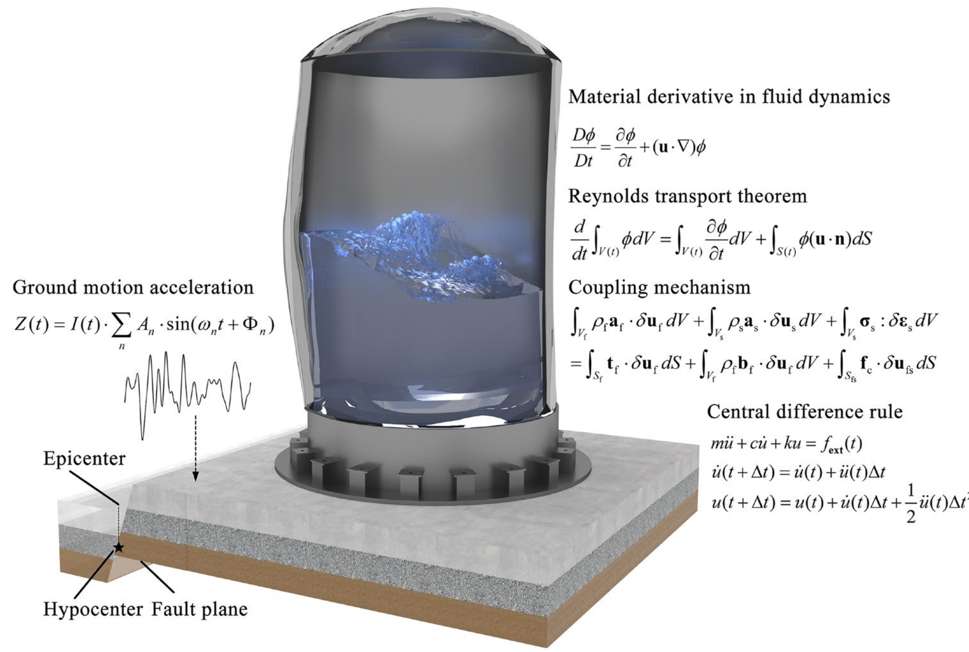

Fig. 1 (Color online) Response of liquid-containing structures during seismic event using the HEL method

Table 2 Overview of key features for FSI numerical simulation methods

Method	Fluid representation	Solid representation	Coupling approach	Computational cost	Accuracy	Typical applications	Unique features
SPH	Lagrangian	Lagrangian	Strong	Moderate	Moderate to high	Free-surface flows Impact problems	Particle-based
DEM	Eulerian/DEM Combination	Discrete particles	Weak	High	Moderate to high	Granular flows Particle-fluid interactions	Particle interactions
IBM	Eulerian	Lagrangian	Weak	Moderate	Moderate	Biofluid mechanics Flexible structures	Simplified coupling
LBM	Mesoscopic	Lagrangian	Weak	Low	Moderate	Porous media Multiphase flows	Mesoscopic modeling
ALE	Eulerian	Lagrangian	Strong	High	High	Large deformations Complex geometries	Mesh flexibility
CEL	Eulerian	Lagrangian	Strong	High	High	Large deformations Extreme loading conditions	Handles fluid–structure interaction Large deformations
SFEM	Eulerian/ALE	Lagrangian	Strong	High	Very high	Problems requiring high accuracy Wave propagation	Higher-order basis functions Spectral convergence
HEL	Eulerian/ALE Combination	Lagrangian	Strong	High	High	Large deformation Impact problems	Combines strengths of CEL & ALE for enhanced seismic analysis

assessment processes, and potentially contributes to a more robust nuclear energy infrastructure.

2 Methods

2.1 Response-spectrum analysis method

The response-spectrum analysis method is essential for evaluating structural responses to transient dynamic events. This characterizes the peak response of a simple harmonic oscillator modeled as a single-degree-of-freedom (SDOF) system under such events [51, 52]. In the absence of external forces, the governing equation for an SDOF system is expressed as:

$$m\ddot{x} + c(\dot{x} - \dot{b}) + k(x - b) = 0. \tag{1}$$

With the introduction of the undamped natural frequency $\omega_0 = \sqrt{\frac{k}{m}}$ and the damping ratio $\xi = \frac{c}{2\sqrt{km}}$, and by focusing on relative displacement, this equation simplifies to:

$$\ddot{x}_{\mathrm{r}} + 2\xi\omega_0\dot{x}_{\mathrm{r}} + \omega_0^2 x_{\mathrm{r}} = -\ddot{b}. \tag{2}$$

Given specific values of ω_0, ξ, and base acceleration $\ddot{b}(t)$, along with initial conditions $x_{\mathrm{r}}(0) = 0$, $\dot{x}_{\mathrm{r}}(0) = 0$, the system's relative displacement $x_{\mathrm{r}}(t)$, velocity $\dot{x}_{\mathrm{r}}(t)$, and acceleration $\ddot{x}_{\mathrm{r}}(t)$, as well as the absolute acceleration $\ddot{x}(t)$, can be calculated. The acceleration spectrum $S_{\mathrm{a}}(\omega_0, \xi, \ddot{b}(t))$ denotes the maximum relative acceleration resulting from the ground acceleration.

For multi-degree-of-freedom systems, eigenmode analysis followed by modal superposition simplifies the system into decoupled modal equations. Each mode j is represented by

$$\ddot{q}_j + 2\xi\omega_j\dot{q}_j + \omega_j^2 q_j = -\phi_j^{\mathrm{T}} M\ddot{b}. \tag{3}$$

The maximum amplitude for mode j, when subjected to a load in the direction n, leverages the response spectrum at the natural frequency ω_j and a structural participation factor Γ_{nj} to yield $\hat{q}_{nj}$. This methodology highlights the combination of the response-spectrum value and participation factor as the key to determining the peak amplitude of an eigenmode. The application of this analysis considers multiple natural frequencies within the range of the design spectrum, which requires amalgamation of the responses. The final step involves combining the modal responses to calculate the physical quantities of interest using the appropriate modal combination methods.

The response-spectrum method is a widely recognized and accepted approach for seismic analysis, and is extensively utilized in various industries, including chemical engineering, civil construction, and nuclear power plant design [53–55]. Its widespread adoption has been reflected in its incorporation into numerous international building codes and standards. For instance, it is a critical component of the seismic design procedures in Eurocode 8 that provides guidelines for designing earthquake-resistant structures across Europe [56]. This method is prominently featured in the American Society of Civil Engineers' ASCE 7-16 standard, which sets minimum design loads for buildings and other structures in the United States [57]. The International Building Code incorporates ASCE 7 as a reference for seismic design provisions, including response-spectrum analysis [58]. The popularity of this method stems from its ability to estimate structural responses to earthquake excitations, making it particularly valuable for the design stages and safety assessments. Its widespread acceptance and proven track record in various fields make it an ideal benchmark for comparison with newer analytical methods such as the HEL method proposed in this study.

2.2 Ground motion acceleration synthesis

This study employs a synthetic approach to generate artificial ground motions, aiming to simulate earthquakes' transient and dynamic nature accurately. This methodology integrates the modification of an initial random process guided by a predetermined Power Spectral Density Function (PSDF) and enveloped within a user-selected shape [59]. This approach ensures that the generated ground motions possess the requisite statistical properties and dynamic characteristics that are reflective of actual seismic events.

The PSDF, which is calculated based on a predefined velocity target spectrum (S_{v}), plays a fundamental role in the synthetic method. This step is critical because the PSDF encapsulates the frequency content necessary to simulate realistic earthquake motions. Subsequently, the ground motion is synthesized by adding sinusoidal waves, each with specific amplitudes (A_n) and phase angles (Φ_n), as follows:

$$X(t) = \sum_n A_n \cdot \sin(\omega_n t + \Phi_n), \tag{4}$$

where $X(t)$ represents the artificial ground motion at time t, ω_n is the angular frequency, and n denotes the nth sinusoidal wave in series. This formulation ensures that the simulation captures the periodic nature of the seismic waves, representing a wide range of earthquake scenarios. To reflect the transient characteristics of earthquakes accurately, stationary sinusoidal processes were modulated by a deterministic envelope, $I(t)$, chosen from the envelope shape module. This modulation results in an artificial ground motion, $Z(t)$, embodying both the temporal and spectral features of seismic events:

$$Z(t) = I(t) \cdot \sum_n A_n \cdot \sin(\omega_n t + \Phi_n). \tag{5}$$

The amplitude vectors and phase angles were systematically varied to simulate different earthquake profiles, maintaining the same overall spectral characteristics but different temporal properties.

The generation of artificial acceleration is inherently iterative and aims to refine the simulated ground motion until it aligns closely with the target response spectrum. This iterative process involves adjusting the PSDF by comparing the desired and computed response spectra at the control frequencies. The adjustment is governed by

$$G(\omega)_{i+1} = G(\omega)_i \left(\frac{S_{\mathrm{v}}^{(\omega)}}{S_{\mathrm{v}(\omega)}^{(i)}} \right)^2, \tag{6}$$

where $G(\omega)_{i+1}$ denotes the recalculated PSDF. This iterative refinement continues until the response spectrum of the generated motion closely matches the target spectrum, thereby ensuring that the synthetic ground motion is statistically valid and representative of the modeled seismic risk profile.

2.3 HEL method

To accurately reflect the mechanics involved in transitioning between the Lagrangian and Eulerian descriptions for FSIs, we focus on two pivotal concepts, viz. the material derivative and continuity equation, alongside the utilization of the Reynolds transport theorem for bridging the gap between the two descriptions [60, 61].

2.3.1 Material derivative in fluid dynamics

The material or substantial derivative links the Eulerian and Lagrangian descriptions by describing the rate of change of a fluid property (e.g., velocity and density) experienced by a moving particle:

$$\frac{D\phi}{Dt} = \frac{\partial \phi}{\partial t} + (\mathbf{u} \cdot \nabla)\phi, \tag{7}$$

where $\frac{D\phi}{Dt}$ is the material derivative of the property ϕ, $\mathbf{u}$ is the velocity field, and $\nabla\phi$ is the gradient ϕ. This equation captures the temporal change in ϕ at a fixed location and the change due to the motion of the fluid itself, aligning with the Eulerian viewpoint while describing the Lagrangian particle dynamics.

2.3.2 Continuity and momentum equations

Reynolds Transport Theorem (RTT) plays a crucial role in converting between system (Lagrangian) and control volume (Eulerian) approaches. This allows the application of conservation laws (mass, momentum, and energy) over a control volume that encompasses the moving system, effectively bridging the gap between the descriptions:

$$\frac{\mathrm{d}}{\mathrm{d}t} \int_{V(t)} \phi \,\mathrm{d}V = \int_{V(t)} \frac{\partial \phi}{\partial t} \,\mathrm{d}V + \int_{S(t)} \phi(\mathbf{u} \cdot \mathbf{n}) \,\mathrm{d}S, \tag{8}$$

where $V(t)$ and $S(t)$ are the time-dependent volume and surface enclosing the fluid or structure, $\mathbf{u}$ is the velocity of the fluid relative to surface S; and $\mathbf{n}$ is the outward unit normal to S.

2.3.3 Coupling mechanism via virtual work

The coupling of fluid and structure in FSIs through the virtual work principle involves ensuring that the sum of all virtual work contributions equals zero, which reflects the equilibrium state. This principle can be expressed through the virtual work equation, which, in its generalized form for FSIs, is as follows:

$$\begin{aligned} &\int_{V_{\mathrm{f}}} \rho_{\mathrm{f}} \mathbf{a}_{\mathrm{f}} \cdot \delta \mathbf{u}_{\mathrm{f}} \,\mathrm{d}V + \int_{V_{\mathrm{s}}} \rho_{\mathrm{s}} \mathbf{a}_{\mathrm{s}} \cdot \delta \mathbf{u}_{\mathrm{s}} \,\mathrm{d}V + \int_{V_{\mathrm{s}}} \boldsymbol{\sigma}_{\mathrm{s}} : \delta \boldsymbol{\varepsilon}_{\mathrm{s}} \,\mathrm{d}V \\ &= \int_{S_{\mathrm{f}}} \mathbf{t}_{\mathrm{f}} \cdot \delta \mathbf{u}_{\mathrm{f}} \,\mathrm{d}S + \int_{V_{\mathrm{f}}} \rho_{\mathrm{f}} \mathbf{b}_{\mathrm{f}} \cdot \delta \mathbf{u}_{\mathrm{f}} \,\mathrm{d}V + \int_{S_{\mathrm{fs}}} \mathbf{f}_{\mathrm{c}} \cdot \delta \mathbf{u}_{\mathrm{fs}} \,\mathrm{d}S, \end{aligned} \tag{9}$$

where V_{f} and V_{s} denote fluid and solid volumes, respectively. ρ_{f} and ρ_{s} are the fluid and solid densities, respectively. $\mathbf{a}_{\mathrm{f}}$ and $\mathbf{a}_{\mathrm{s}}$ are the acceleration fields of the fluid and solid, respectively. $\delta\mathbf{u}_{\mathrm{f}}$ and $\delta\mathbf{u}_{\mathrm{s}}$ represent the virtual displacements of the fluid and solid, respectively. $\boldsymbol{\sigma}_{\mathrm{s}}$ denotes the stress tensor of the solid. $\delta\boldsymbol{\varepsilon}_{\mathrm{s}}$ denotes the virtual strain tensor of the solid. S_{f} is the surface on which the external tractions $\mathbf{t}_{\mathrm{f}}$ act on the fluid. $\mathbf{b}_{\mathrm{f}}$ represents the body force per unit mass (e.g., gravity) acting on a fluid. S_{fs} is the interface surface between the fluid and solid. $\mathbf{f}_{\mathrm{c}}$ is the contact force of the fluid-solid interface per unit area. $\delta\mathbf{u}_{\mathrm{fs}}$ represents the virtual displacement at the fluid-solid interface.

The penalty function method is applied at the fluid–structure interface (S_{fs}) to enforce the compatibility and no-penetration constraints as

$$\mathbf{f}_{\mathrm{c}} = k_{\mathrm{c}} \Delta \mathbf{u}_{\mathrm{fs}}, \tag{10}$$

where k_{c} denotes the penalty stiffness coefficient that enforces the constraint, $\Delta\mathbf{u}_{\mathrm{fs}}$ denotes the relative (penetration) displacement between the fluid and solid at the interface, which should be minimized.

This equation ensures that any penetration between the fluid and solid is resisted by a force proportional to the penetration depth, effectively coupling the fluid and solid domains through the virtual work performed by the contact forces. This mechanism allows for consistent and physically accurate interactions between the fluid and solid phases in the simulations, enabling the practical analysis of complex FSI within the HEL method framework.

3 Analysis of methods

3.1 Response-spectrum analysis of seismic

3.1.1 Configuration of optimization

The response-spectrum method is a foundational analytical tool in the seismic analysis of liquid-containing structures for nuclear reactor systems. In this study, we employ a parametric approach to investigate the sensitivity of the seismic response to key structural and liquid parameters using response-spectrum analysis, a method widely applied in seismic optimization studies [62]. This study is focused on vertical storage tanks, which are critical components of nuclear facilities, and evaluates three primary parameters: liquid level, tank height, and wall thickness. This parametric study aims to quantify the influence of structural parameters on the seismic response, while simultaneously assessing the impact of liquid parameter variations on the seismic behavior of vertical tanks.

Figure 2a illustrates the study's structural analysis and optimization flowchart. The structural system under investigation comprises a tank body, skirt supports, and upper and lower butterfly heads. The focus of this research is on the wall thickness, which varies from 5 mm to 60 mm, explicitly targeting the sections of the tank in direct contact with the contained liquid. The tank height is adjusted from 7 m to 12 m; however, these modifications do not change the support structures. Specifically, the height of the skirt support structure is 0.6 m, and its thickness is 50 mm throughout the analysis. The design strategically sets the liquid level within the tank to accommodate a range between 0 m and 6.4 m, ensuring that it covers all potential tank volumes. Utilizing the central composite design (CCD), a comprehensive set of parametric design models is generated. These models are evaluated using the kriging response surface methodology, which is a robust technique for modeling and analyzing complex systems [63, 64]. The evaluation criteria encompass a variety of indicators, such as modal shape and frequency, maximum equivalent stress sustained by the structure, and total displacement under seismic conditions.

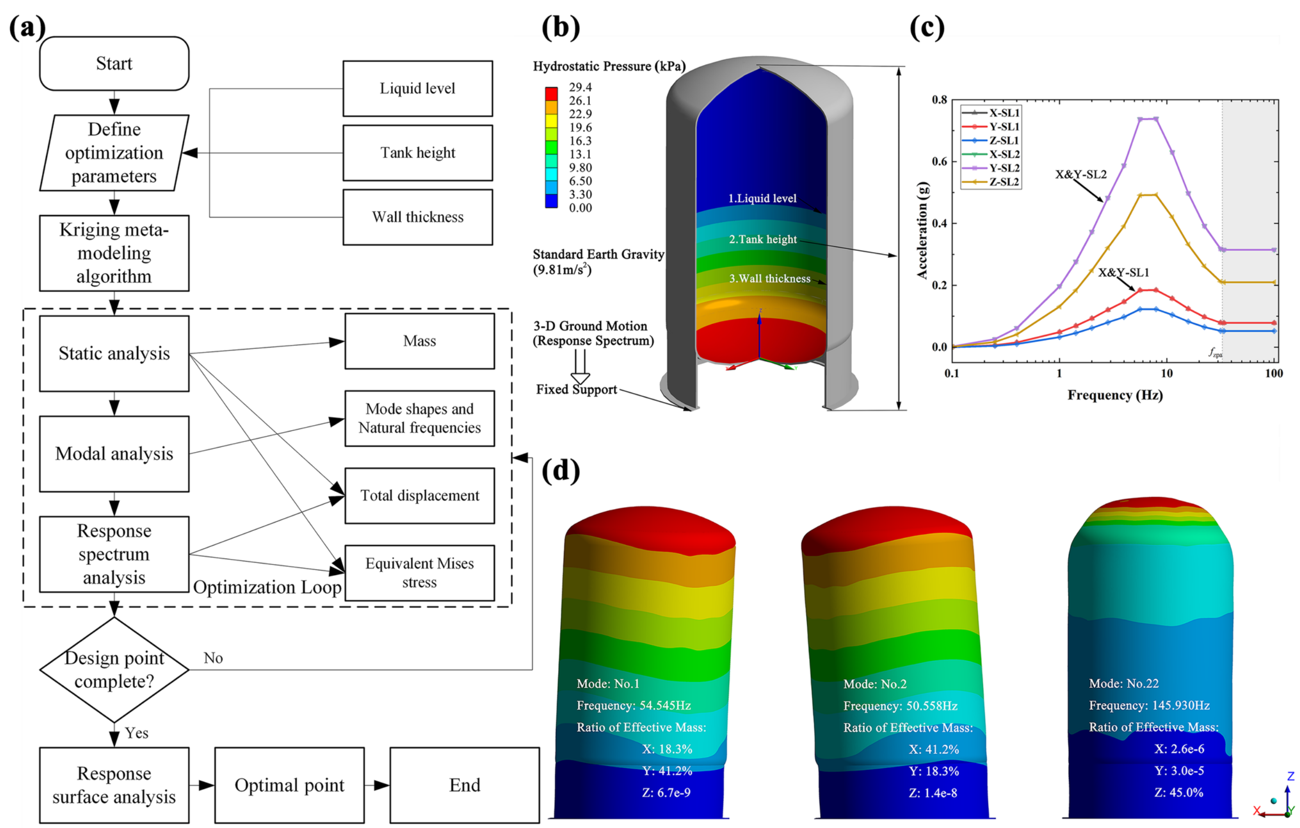

Fig. 2 (Color online) Response of liquid-containing structures during seismic event using the response-spectrum method. **a** Structural analysis and optimization flowchart; **b** Boundary conditions of the response-spectrum analysis; **c** Horizontal and vertical response spectrum of 5% damping; **d** Dominant structural modes with significant modal mass ratios in principal directions

The loads impacting the structural system include gravity and hydrostatic pressure, with the structural base secured by fixed supports, as shown in Fig. 2b. Seismic response analysis is conducted based on the response spectra of the equipment close to the ground, as shown in Fig. 2c [65–67]. While conventional structural design often utilizes standard code-based spectra, such as those from ASCE to 7-16 [57], in this study, we employ a specific spectrum obtained from ITER documentation. This approach is justified by the unique requirements of nuclear facilities, which necessitate more stringent seismic safety considerations that align with international standards for nuclear safety, such as those published by the International Atomic Energy Agency (IAEA) [68].

Figure 2c illustrates the seismic response spectrum derived from ITER documentation and used in this analysis. The spectrum incorporates two seismic levels: Seismic Level 1 (SL-1) and Seismic Level 2 (SL-2), which are defined by the IAEA for nuclear power plant design. SL-2, equivalent to the Safety Shutdown Earthquake, represents the maximum potential earthquake for which the plant must safely shut down. SL-1, corresponding to the Operating Basis Earthquake, denotes the seismic level at which the plant should remain operational. In the context of ITER, SL-2 is used to design safety-important structures, systems, and components, whereas SL-1 is applied to conventional structures and systems. Due to the rotational axis symmetry inherent in the structural design, the seismic responses in the X and Y directions are assumed to remain consistent under the same seismic intensity. This assumption is crucial as the focus is on the methodologies, not on the impact of varying response-spectrum amplitude or parameters. Selecting a universal response spectrum ensures that the findings are widely applicable and relevant to the method's generalizability while adhering to the specialized requirements of nuclear facility design.

To further characterize the structural behavior under seismic conditions, a modal analysis was performed. Figure 2d shows the modal analysis results, highlighting the dominant structural modes in the principal directions. The analysis reveals the modes with significant modal mass ratios, providing insight into the structure's dynamic behavior under prestressed conditions.

The material properties of both the solid and fluid components, which are critical for the seismic analysis, are presented in Table 3. Figure 3 shows the minimum and average true stress–strain curves for the 304 stainless steel, providing critical insights into the material's behavior under dynamic conditions.

The response-spectrum analysis method for assessing the seismic response of storage tanks in nuclear reactors has provided insights into their dynamic behavior. We used complete quadratic combination and square root of sum of squares to aggregate periodic vibration modes, while the missing mass method summed rigid body modes. These methods enable analysis by accounting for multiple vibrational modes. The analysis, considering frequencies from 0 Hz to 240 Hz, includes periodic and rigid modes. The selected frequency range ensures that the structural natural frequency remains distant from the seismic frequency of 33 Hz, effectively reducing the impact of seismic events.

Table 3 Material properties of components in the analysis

Material	Parameter	Value
316 L (20°C, 1 atm)	Density	7930 kg/m^3
	Young's modulus	200 GPa
	Poisson's ratio	0.3
	Plastic parameters	Refer Fig. 3 for details
	Speed of sound	5265 m/s
Water (20°C, 1 atm)	Density	1000 kg/m^3
	Dynamic viscosity	0.001 Pa·s
	Speed of sound	1483 m/s

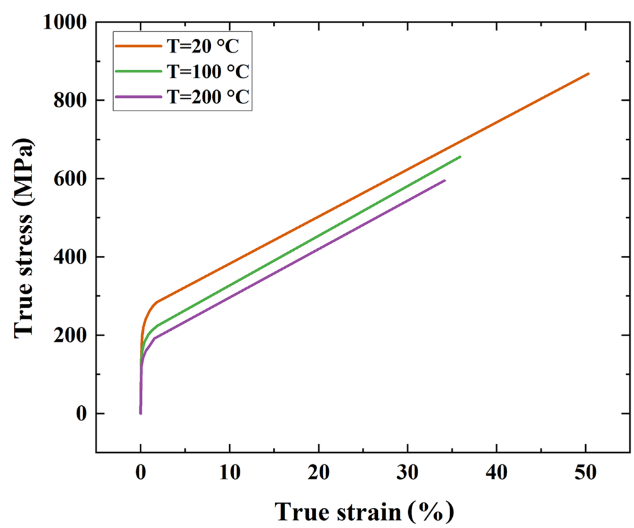

Fig. 3 (Color online) Minimum and average true stress–strain of 316 L

3.1.2 Results and discussion

The sensitivity of the structural response to various parameters under different design conditions is depicted in Fig. 4. This sensitivity distribution diagram illustrates the positive and negative correlations of parameters such as tank height and liquid level with the seismic response indicators. The tank height significantly influences the evaluation and optimization parameters, whereas the liquid level has minimal impact on the structural modes. This observation aligns with the results obtained from the prestressed modal analysis,

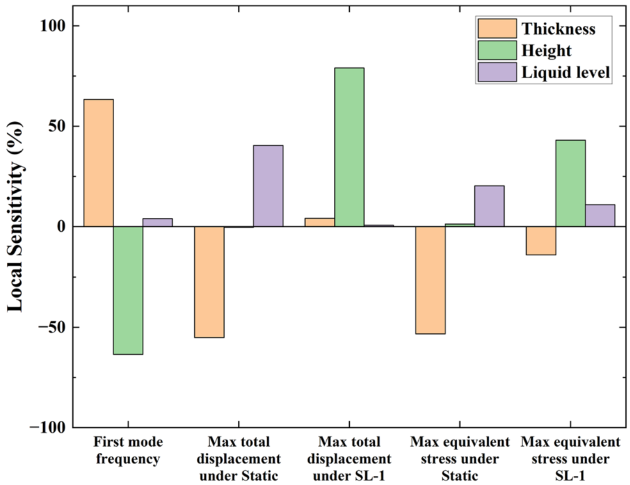

Fig. 4 (Color online) Sensitivity distribution diagram

indicating that the static load response predominantly determines the structural response under seismic conditions.

The analysis results are clearly depicted on the response surface, as illustrated in Fig. 5. This visualization delineates the influence of each study parameter on the seismic performance targets. These insights provide a quantitative basis for the ongoing optimization of tank structural designs, with the aim of enhancing their safety and efficacy under seismic conditions.

The tank wall thickness and height response surfaces against seismic performance indicators, such as the first-order mode, structural displacement, and stress, are depicted in Fig. 5a–Fig. 5c. These visualizations show the influence of parameters on seismic performance targets. Figure 5a shows that tank body height dominates the first-order natural frequency under prestress. When the tank height is high enough, the first-order natural frequency will be close to or lower than the rigid body frequency of 33 Hz, implying that earthquakes have a negligible effect on low-height tanks. Combining Fig. 5b and Fig. 5c, we observe that the normalized seismic response under stress prestressing mode can be represented by maximum relative displacement and maximum equivalent stress. This result does not combine structural self-weight condition responses, only seismic ones. These insights provide a basis for optimizing tank structural designs to enhance safety under seismic conditions. By analyzing these parameters, this investigation characterizes the tank's seismic response, contributing to understanding dynamic behavior of liquid-containing structures in nuclear facilities.

We identified the optimal structural parameters for tank design: a height of 7 m corresponding to highest natural frequency, wall thickness of 30 mm for structural integrity, and liquid level of 4.8 m (75% of internal height). These parameters, selected based on preliminary tests, provide a foundation for future tank design and safety assessments. The modal mass analysis shown in Fig. 6 reveals the concentration of the modal mass within the first two modes on a logarithmic scale. This concentration indicates the initial modes' critical role in the seismic response, with the dominant mode at a characteristic frequency of 145 Hz classified as rigid owing to its high frequency relative to the periodic modes.

The tank's maximum displacement and equivalent stress levels are analyzed, and the specific locations of these maxima are identified and documented in Table 4. These findings provide a basis for evaluating structural safety and reliability according to the criteria of the RCC-MR [69] code or ASME VIII Div. 1 [70] and Div. 2 [71]. This evaluation is crucial to ensure the integrity and safety of nuclear reactor components under seismic conditions.

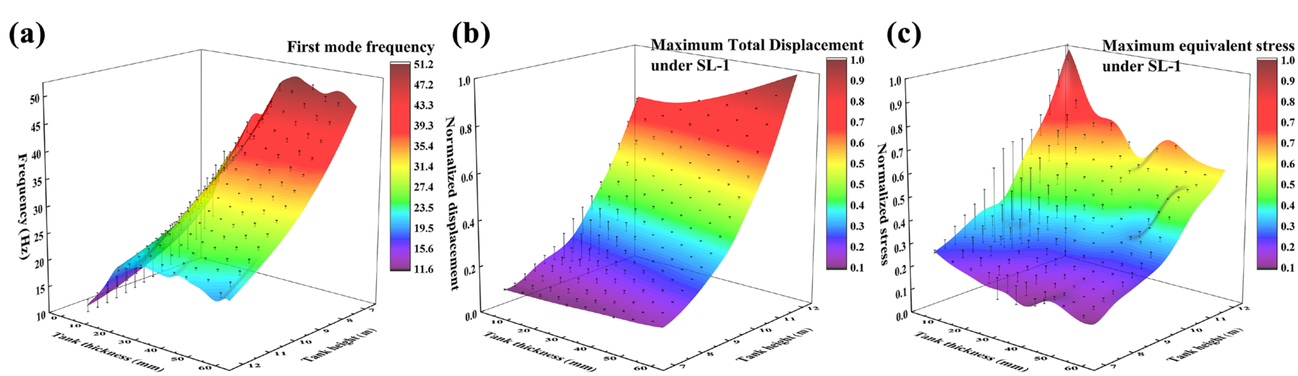

Fig. 5 (Color online) Structural response from response-spectrum analysis with error bars representing variability due to liquid-level height. **a** First mode frequency; **b** Total displacement; **c** Equivalent stress

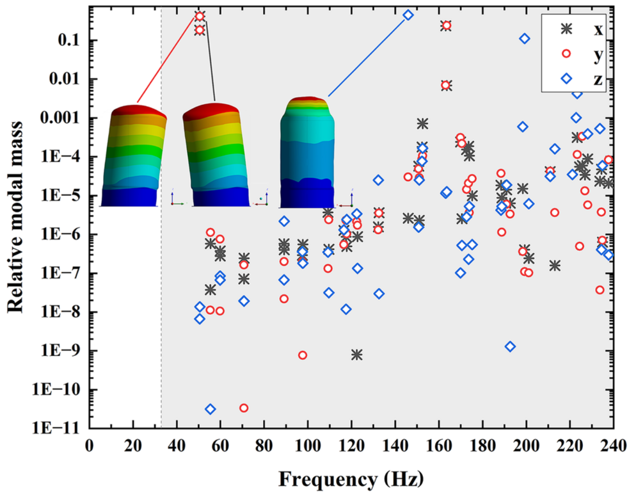

Fig. 6 (Color online) The relative modal mass as a function of eigenfrequency

3.2 Time-history analysis of seismic

3.2.1 Implementation of the HEL method model

This study utilizes the HEL method to evaluate the dynamic responses of a liquid-containing structure under seismic excitation. This modeling approach divides the system into two computational domains: the Euler domain, which represents the fluid dynamics within the tank, and the Lagrangian domain, which simulates the structural dynamics of the tank, as shown in Fig. 7. The integration of these domains enables a detailed representation of FSI under seismic loading, capturing both the complex motion of the fluid and structural deformation.

The Euler domain simulates fluid behavior under seismic excitation through a finely meshed Eulerian grid, capturing wave propagation, sloshing, and pressure distribution. The Lagrangian domain models the tank's structural response using a refined mesh for precise simulation of deformation, stress distribution, and stability during seismic events.

Three observation points monitor the seismic response: the top observation point, liquid-level side point, and dynamic peak point. The top observation point, located at the tank's highest edge, tracks global displacement and deformation under seismic excitation, providing insights into structural performance and stability.

The liquid-level side point corresponds to the maximum liquid level under dynamic conditions, moving with changes in liquid height caused by seismic forces. The point position tracks within ±25% of the static initial liquid height to represent the liquid's fluctuating behavior throughout the seismic response.

Table 4 Assessment of maximum displacement and equivalent stress under diverse conditions (Tank parameter: Tank height: 7 m, wall thickness: 30 mm, liquid level: 75% of the tank's internal height)

Load	Condition	Maximum total displacement (mm)	Location	Maximum equivalent stress (MPa)	Location
Statics	Hydrostatic pressure and gravity	0.216	Bottom of tank	5.434	Connection between skirt support and tank
Dynamics	Seismic (SL-1)	0.016	Top of tank	0.314	
Combinations	Statics and dynamics	0.217	Bottom of tank	5.443	

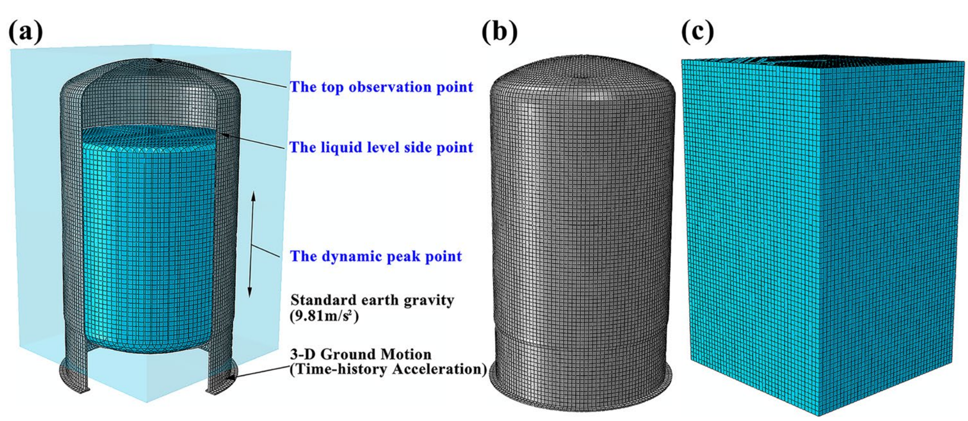

Fig. 7 (Color online) Seismic time-history analysis model for structural dynamics. **a** Boundary conditions and markers for the three observation points; **b** Lagrangian domain; **c** Eulerian domain

The dynamic peak point represents the location within the Lagrangian domain where the maximum structural response occurs under seismic excitation. This point varies with time depending on the dynamic interaction between the fluid and structure, capturing the peak displacement or stress experienced by the tank walls during the seismic event. Identifying this point is crucial for assessing the structural safety and integrity of the tank as it provides insights into the areas experiencing the highest strain and potential failure risks.

By carefully defining these three observation points, the HEL method can effectively capture the global and localized seismic responses of the system, thereby enabling a comprehensive evaluation of the FSI. This approach provides a robust and secure framework to accurately simulate the complex dynamics of liquid-containing structures subjected to seismic loading.

The primary function of the Euler domain is to simulate fluid behavior under seismic excitation, emphasizing the need for a finely meshed Eulerian grid to accurately capture intricate fluid phenomena. Conversely, the structural response of the tank encapsulated within the Lagrangian domain necessitates a similarly detailed mesh to ensure the precision of the structural dynamics simulations.

The synergy between these domains through Euler–Lagrange coupling offers a nuanced understanding of the interplay between fluid dynamics and structural integrity under seismic loading. This methodology enhances the accuracy of seismic response predictions and provides a comprehensive framework for analyzing the complex interactions inherent in fluid–structure systems.

3.2.2 Grid independence analysis

Grid independence analysis is critical in numerical simulations to ensure mesh size does not unduly influence results. The objective is to identify an optimal mesh resolution balancing computational efficiency and solution accuracy. We used the response surface method to assess mesh size impacts in Eulerian and Lagrangian domains on FSI dynamics within the HEL method. The simulation involves a tank filled to 75% with liquid under gravitational loading to analyze fluid–structure interaction. The HEL method captures this dynamic interaction effectively. Figure 8 shows the grid independence analysis results, illustrating mesh size effects on calculation cost and structural response, focusing on maximum displacement and stress.

Three key metrics evaluated mesh adequacy: calculation cost, maximum displacement, and maximum stress. A static analysis under hydrostatic pressure and gravity was performed alongside the dynamic HEL simulation, serving as a baseline for comparison, represented by the blue curve in the X-Z plane in Fig. 8. The results show mesh resolution's importance in the Lagrangian domain for accurate structural response. In both methods, maximum displacement and stress occurred at the tank bottom's geometric center, though magnitudes varied between analyses due to different loading conditions. The calculation cost of the HEL method FSI simulation, shown in Fig. 8a, depends heavily on mesh sizes in both domains. When the Eulerian domain has small mesh while the Lagrangian domain remains coarse, computational time increases significantly with potential convergence issues. This discrepancy is observed because the Eulerian domain needs finer resolution for accurate fluid dynamics modeling. As shown in Fig. 8b and Fig. 8c, while simulation shows approximate convergence at larger grid sizes around 800 mm, the convergence is weak and rapidly diverges with further refinement. This phenomenon suggests that coarse meshes may not be sufficient to resolve the intricate FSI accurately, particularly in transient analyses, as larger mesh sizes smooth out critical interaction details (leading to inaccurate predictions of structural responses).

As the mesh is refined, the grid sizes of Eulerian and Lagrangian domains must be matched and sufficiently refined for convergence and accuracy in HEL simulations.

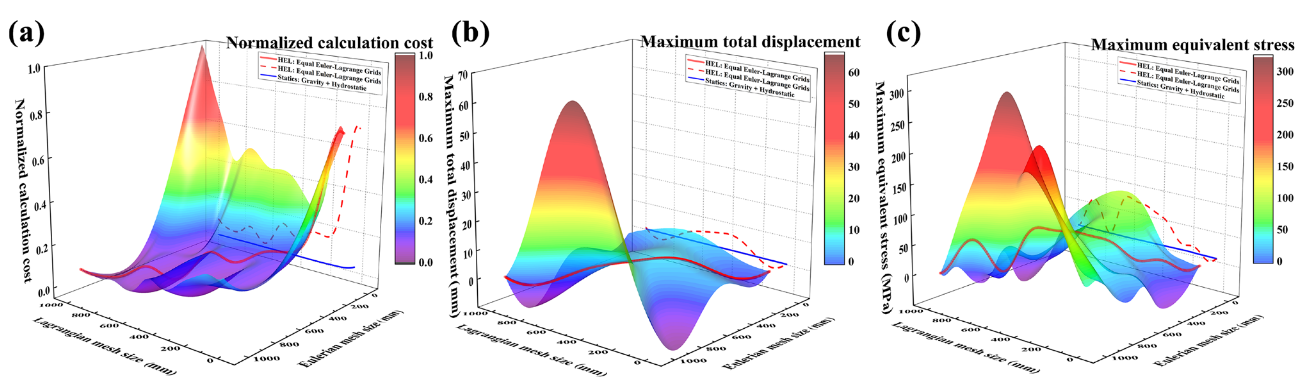

Fig. 8 (Color online) Response of liquid-containing structures during the seismic event using the HEL method. **a** Calculation cost; **b** Total displacement; **c** Equivalent stress

A mesh size of approximately 200 mm in both the domains balances the calculation cost and accuracy. Optimal results are achieved when the Eulerian domain uses a mesh size of 100 mm × 100 mm × 100 mm and the Lagrangian domain uses 80 mm × 80 mm × 80 mm. This correspondence between grid sizes is crucial for accurate fluid–structure coupling and reliable outcomes.

Figure 9 presents tank liquid levels from empty to high, designated as L1 through L4. This classification enables assessment of how liquid levels affect dynamic response and structural stresses under seismic conditions. The analysis is crucial, as liquid presence can alter stress distribution and deformation patterns. This classification helps formulate safety measures and enhance liquid storage facility design in nuclear reactors.

The modeling area consists of two domains, as shown in Fig. 7: the "Tank" represents the Lagrangian domain, while the "Whole fluid domain" represents the Euler domain encapsulating it. As detailed in Table 5, the grid sizes in both domains are matched to maintain solution accuracy. The Lagrangian domain contains two layers of grids in the thickness direction to capture the tank's structural dynamics during seismic response. Liquid phases L1 through L4 in Table 5 serve only as initialization parameters and reflect material volume fractions within the mesh. The Euler domain's grid size remains constant while fluids flow between grids, interacting with structure and fluid, whereas the Lagrangian domain follows material motion. The Courant–Friedrichs–Lewy (CFL) condition stays below one to ensure numerical stability.

3.2.3 Ground motion acceleration synthesis

Ground motion selection is crucial in time-history dynamic analysis, with multiple recorded motions used for average structural responses. We used synthetic records from the ITER-specific response spectrum, ensuring consistency with the response-spectrum analysis and confirming direct comparability between the HEL and response-spectrum methods. The ITER spectrum reflects seismic hazard considerations for nuclear facilities that recorded motions may not represent. Synthetic records enable control over frequency content and duration, ensuring alignment with the design spectrum. For this study's specific site and hazard level, recorded ground motions may inadequately match the target spectrum without excessive scaling. The study aims to compare the HEL method with the response-spectrum method, using synthetic records to maintain consistency while accurately reflecting the facility's design basis. This approach enables direct evaluation of the HEL method in fluid–structure interaction analysis.

Following the ground motion acceleration synthesis methodology (described in "Method"), in this study, we develop the intensity function using the Saragoni & Hart envelope [72], which characterizes seismic wave maximum amplitude over time. This generates representative seismic input within the $I(t)$ envelope, as shown in Fig. 10. The time–acceleration curves for SL-1 scenario show horizontal peak ground acceleration of 0.060 g and vertical peak acceleration of 0.045 g. The generated motions maintain an average error below 10%, demonstrating high fidelity in synthetic accelerogram representation.

The structural form in this section aligns with the structure described in Table 4. The primary analysis condition includes 75% of the tank's internal height specified in Table 5, corresponding to the L4 liquid level. This condition examines the structural performance under significant load. The structure is also analyzed under three other liquid-level conditions to ensure comprehensive understanding across operational scenarios, ensuring robust conclusions.

3.2.4 Results and discussion

The analysis of fluid sloshing and structural response under seismic excitation provides insights into the dynamic interaction between liquid and tank structure. Figure 11 presents curves showing the temporal variation in maximum sloshing height of liquid within the water tank, analyzed using the HEL method. This graph captures the liquid's dynamic response under seismic excitation. The results indicate that at 4 s, the L4 liquid sloshing height reaches its maximum value, corresponding to the intensity of the synthetic ground

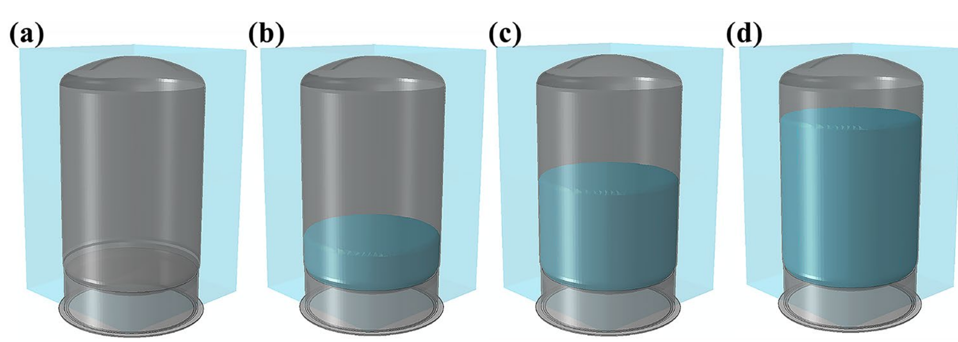

Fig. 9 (Color online) Classification of the structure at various liquid levels. **a** Level L1 (empty), 0.0 m; **b** Level L2 (low), 1.6 m; **c** Level L3 (half), 3.2 m; **d** Level L4 (high), 4.8 m

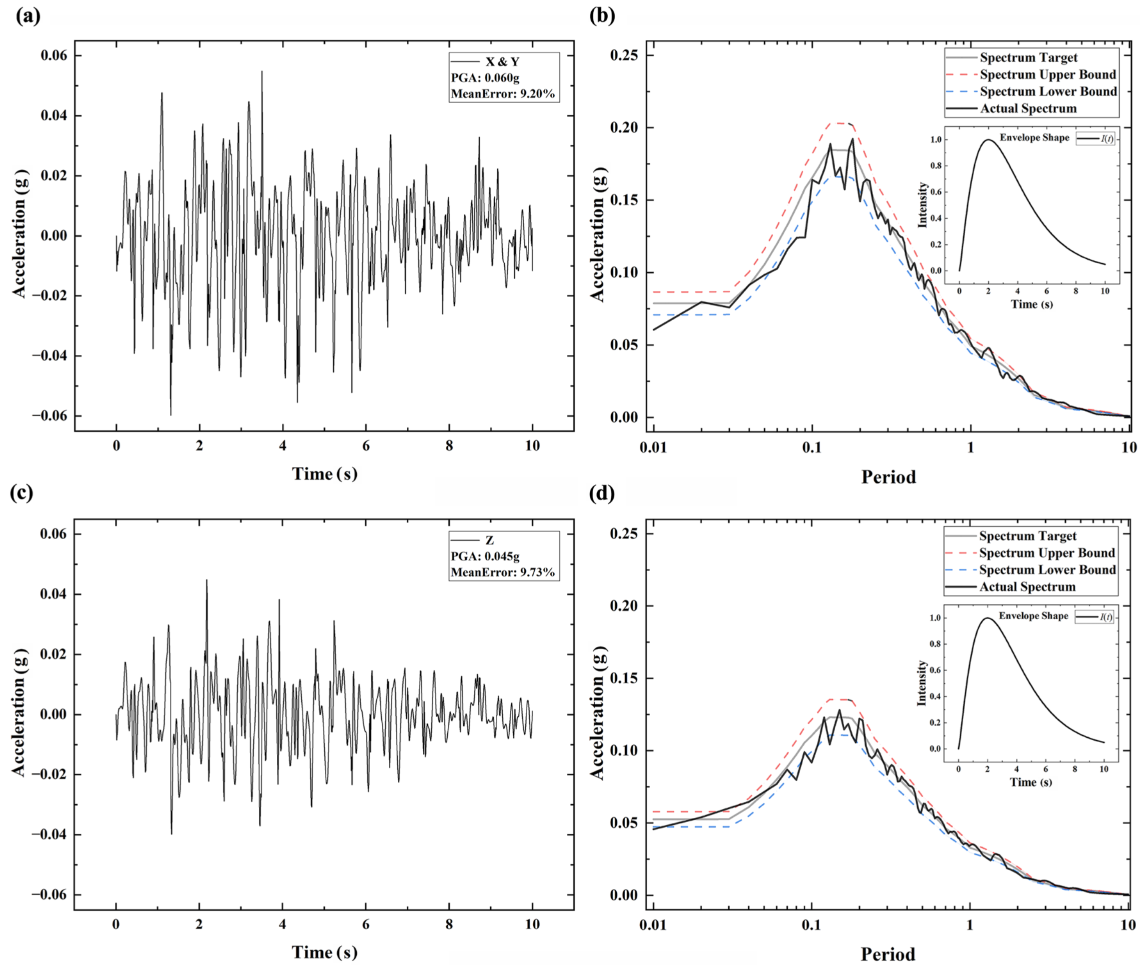

Fig. 10 (Color online) Synthetic ground motion and corresponding response spectra. **a** Acceleration time history in the horizontal direction; **b** Corresponding response-spectrum envelope; **c** Acceleration time history in the vertical direction; **d** Corresponding response-spectrum envelope

Table 5 Finite-element model parameters for the HEL method in seismic response analysis

Component	Material	Domain	Element type	Number of elements	Min element size (mm^3)	Smallest stable time increment (s)	CFL
Tank	316 L	Lagrange	8-node element C3D8R	30816	74.05 × 72.36 × 12.85	1.76×10^{-6}	0.720
Whole fluid domain	Water	Euler	8-node element EC3D8R	118188	100.00 × 100.00 × 100.00		0.026
Liquid of L1	Water	Euler	8-node element EC3D8R	0	100.00 × 100.00 × 100.00		0.026
Liquid of L2	Water	Euler	8-node element EC3D8R	19978	100.00 × 100.00 × 100.00		0.026
Liquid of L3	Water	Euler	8-node element EC3D8R	40410	100.00 × 100.00 × 100.00		0.026
Liquid of L4	Water	Euler	8-node element EC3D8R	59565	100.00 × 100.00 × 100.00		0.026

motion in Fig. 10. In contrast, for the L2 and L3 liquid levels, the maximum values occur around 8 s. This delay may be due to liquid mass inertia and damping effects within the tank structure. The tank of the L1 liquid level is empty, and therefore, no sloshing height exists. These findings demonstrate seismic loading's impact on fluid behavior. The variations in sloshing heights across different liquid levels emphasize the need for assessing fluid–structure interactions during seismic events for optimizing tank design and structural integrity.

A series of snapshots of fluid sloshing within the tank under seismic excitation at two liquid levels were captured at intervals, as shown in Fig. 12. The minimum value for explicit stress in the cloud chart was set at 1 MPa to enhance

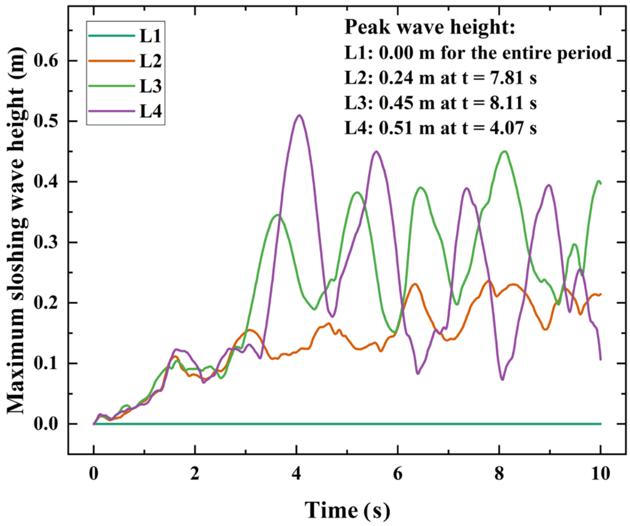

Fig. 11 (Color online) Maximum sloshing wave heights over time under seismic loading based on the HEL method (Smoothed results)

visibility of fluid sloshing effects on structural stresses. These images show stress distribution changes on the tank structure over time. The circumferential stress is uniform below the liquid surface due to hydrostatic pressure. Above the liquid surface, liquid sloshing causes notable changes in structural stress distribution through fluid-wall interaction.

The stress and displacement responses are extracted at 0.01 s intervals, as shown in Fig. 13, using an upper envelope method to standardize structural response curves. Figure 13b and Fig. 13c show higher stress levels at elevated liquid volumes compared to reduced volumes. Using the HEL method, stress values at intermediate to high liquid levels (L2-L4) are approximately double those from response-spectrum analysis. In scenarios without liquid, both methods yield comparable stress magnitudes. This difference occurs due to two factors: increased liquid sloshing amplitude at higher levels enhances fluid inertial forces (shown in Fig. 13d, Fig. 13e, and Fig. 13f), and hydrostatic pressure intensifies at higher fluid levels. While stress levels near the liquid surface do not reach peak levels seen elsewhere, they remain high relative to maximum stress points.

As the seismic event progresses, the relative displacement of the structure peaks between 8 s to 10 s, despite reduced acceleration. This indicates a nonlinear and delayed displacement response, showing cumulative effects under seismic influences. The structural response reflects a complex interplay of factors accumulating over time. This is supported by maximum values observed for L2 and L3 liquid-level sloshing, as shown in Fig. 11. The alignment of these maxima with structural displacement peaks demonstrates fluid dynamics' influence on structural behavior during seismic events. The HEL analysis shows that the average relative displacement at three observation points equals the response-spectrum analysis result, while the peak-to-peak value is approximately twice that of the response-spectrum analysis result. This finding in Fig. 13d, e, f aligns with stress results in Fig. 13b and Fig. 13c for the liquid-containing tank, highlighting the importance of considering

Fig. 12 (Color online) Temporal evolution of structural stress distribution in seismic time-history analysis. **a** Level L3; **b** Level L4

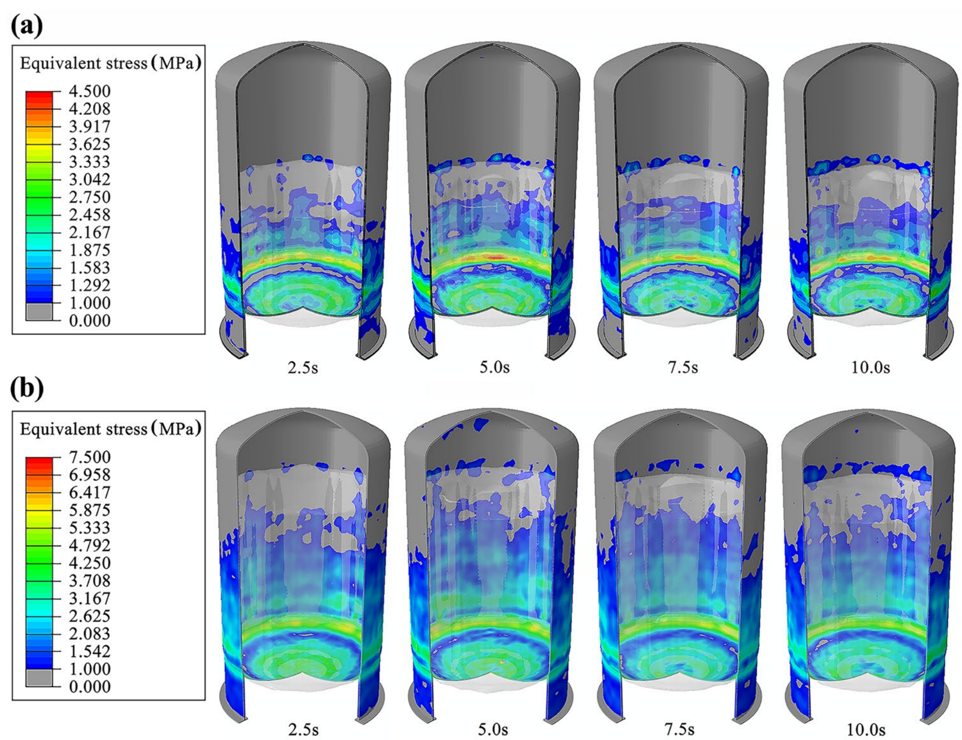

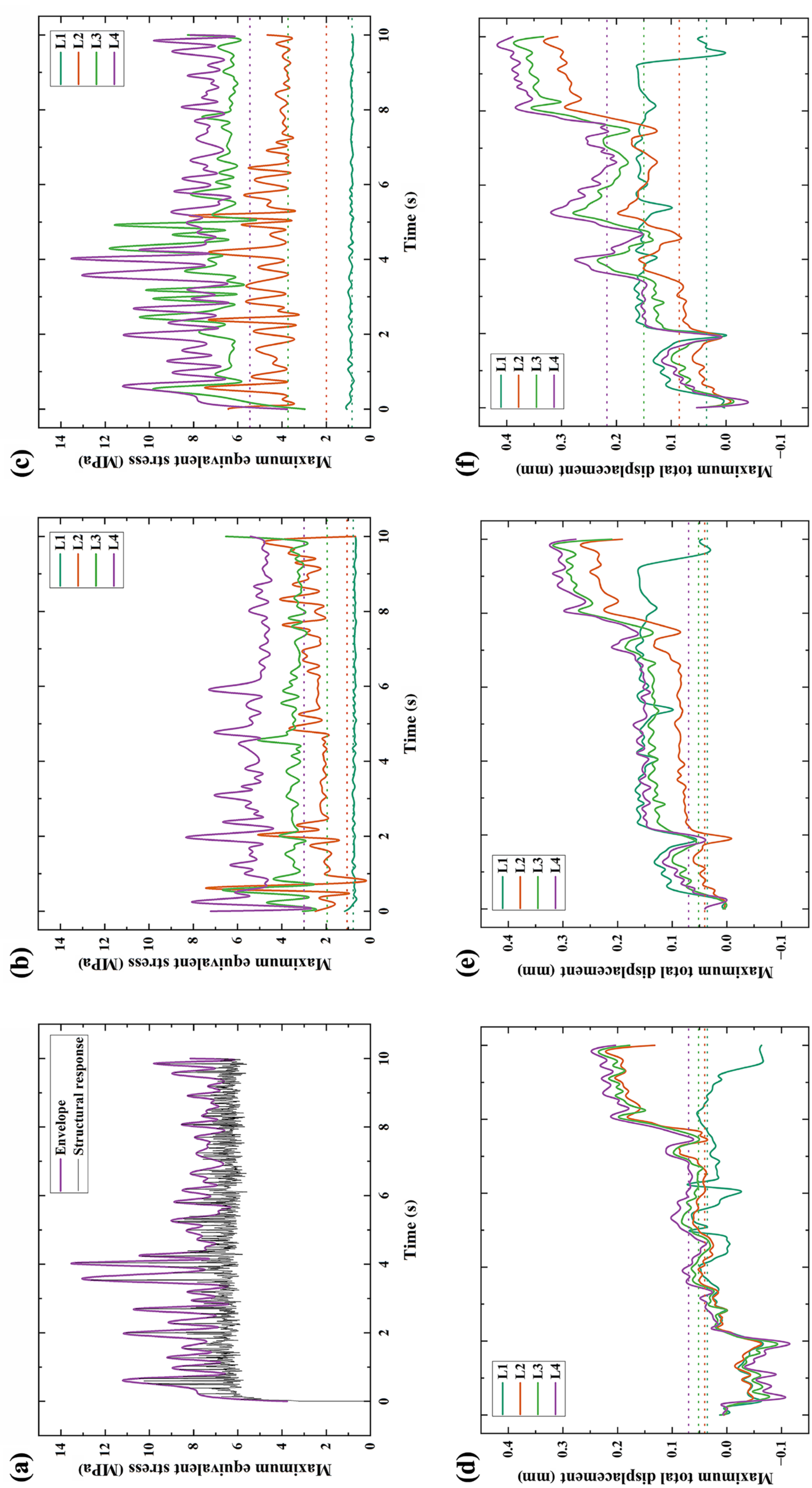

Fig. 13 (Color online) Temporal variation of the maximum stress and displacement of the structure at different liquid levels. **a** Stress response envelope; **b** Stress at the liquid-level side point; **c** Stress at the dynamic peak point; **d** Displacement at the top observation point; **e** Displacement at the liquid-level side point; **f** Displacement at the dynamic peak point. Dotted lines indicate results from the response-spectrum method

both instantaneous and cumulative responses in structural analysis.

Further analysis shows that the structural acceleration response peaks at 2 s (refer to acceleration time–history curve and $I(t)$ envelope in Fig. 10) represent the maximum instantaneous dynamic load from seismic activity. Intriguingly, as shown in Fig. 13d, Fig. 13e, and Fig. 13f, the relative displacement is minimized at this point, indicating that the maximum acceleration occurs at lower displacement values, likely due to phase lag between acceleration and displacement. This minimal displacement suggests a dynamic counter-adjustment within the structure, explored through the HEL method across varying liquid levels.

4 Comparison of methods

The maximum equivalent stress results from the HEL method without liquid, shown in Fig. 13b, c , align with the response-spectrum method results, despite minor temporal variations. This indicates negligible interaction between Eulerian and Lagrangian domains when no liquid is present. The empty Eulerian domain has minimal impact on stress results, making the stress response similar to traditional time-history analysis, with the HEL method effectively capturing stress behavior.

However, with liquid present, as shown in Fig. 13b, c, the maximum equivalent stress from the HEL method is approximately twice that of the response-spectrum method. This difference occurs because the HEL method accounts for fluid–structure interaction, explicitly modeling the coupling between liquid and tank walls, leading to higher stress levels from fluid inertia and hydrodynamic pressure. The response-spectrum method simplifies the system by neglecting this interaction, resulting in lower stress values, highlighting the HEL method's superior capability in modeling fluid–structure coupling under seismic loading.

In contrast, the maximum total relative displacement results in Fig. 13e, f show significant differences between the methods. The HEL method produces larger displacements with greater fluctuations over time due to its time-domain formulation, which captures transient dynamics and high-frequency vibrations often missed by the response-spectrum method. The explicit dynamics algorithm in the HEL method is sensitive to tra'nsient effects and numerical noise, leading to amplified displacements. The response-spectrum method, with its fixed damping ratio, yields smoother displacement responses, while the HEL method shows larger oscillations due to reduced damping effects. These differences highlight the HEL method's ability to capture detailed dynamic behavior. The comparison in Fig. 14a, d shows their advantages in seismic analysis of liquid-containing structures. In practical engineering, structural seismic analysis combines with other working conditions. The response-spectrum method calculates seismic response independently and combines parameters using various methods, potentially causing inconsistencies in load combination processes.

The HEL method allows simultaneous application of various loads, including seismic loads, to the initial structure. This method considers fluid dynamic characteristics, providing accurate representation of real-world conditions. By integrating multiple loads, the HEL method eliminates inconsistencies from separate load combinations, ensuring reliable analysis of structural seismic response.

As shown in Fig. 14b, the response-spectrum method captures structural response to seismic loading. Based on SDOF models, it emphasizes the structure's vibrational characteristics. While providing robust initial assessment, it simplifies fluid dynamics by not accounting for fluid–structure interaction in detail. The method predicts displacement based on predefined vibrational properties, potentially overlooking dynamics from fluid motion. The HEL method (Fig. 14e) incorporates detailed fluid and structural dynamics simulation. Using synthesized seismic acceleration–time spectra, it simulates interaction between structural components and contained fluid. Results indicate displacement patterns opposing foundational movement, showing fluid inertia's influence on structural response. This method captures complex fluid behaviors, including nonlinear surface motions and sloshing. The SDOF model needs to address these adequately. The HEL method provides a comprehensive understanding of dynamic velocity and structural interactions during seismic events. The analysis shows the limitations of the response-spectrum method in complex FSI scenarios; it fails to account for dynamic pressures and fluid motion effects. The HEL method reveals that fluid inertia can alter structural response, either acting as a damping force or enhancing response amplitude. This comparative analysis demonstrates that the HEL method provides a superior framework for understanding the intricate dynamics of liquid-containing structures under seismic loads. By accounting for FSI, it offers a more precise prediction of structural behavior, which is essential for designing safer nuclear facilities.

5 Conclusion

The comparative analysis between the response-spectrum and HEL methods reveals an evolution in seismic safety assessment of liquid-containing structures in nuclear reactors. The traditional response-spectrum analysis fails to accurately capture dynamic responses of structures critical to the operational safety of nuclear systems, such as vacuum pressure relief and cooling water system tanks. Our findings reveal that the response-spectrum method significantly underestimates the maximum structural stress and

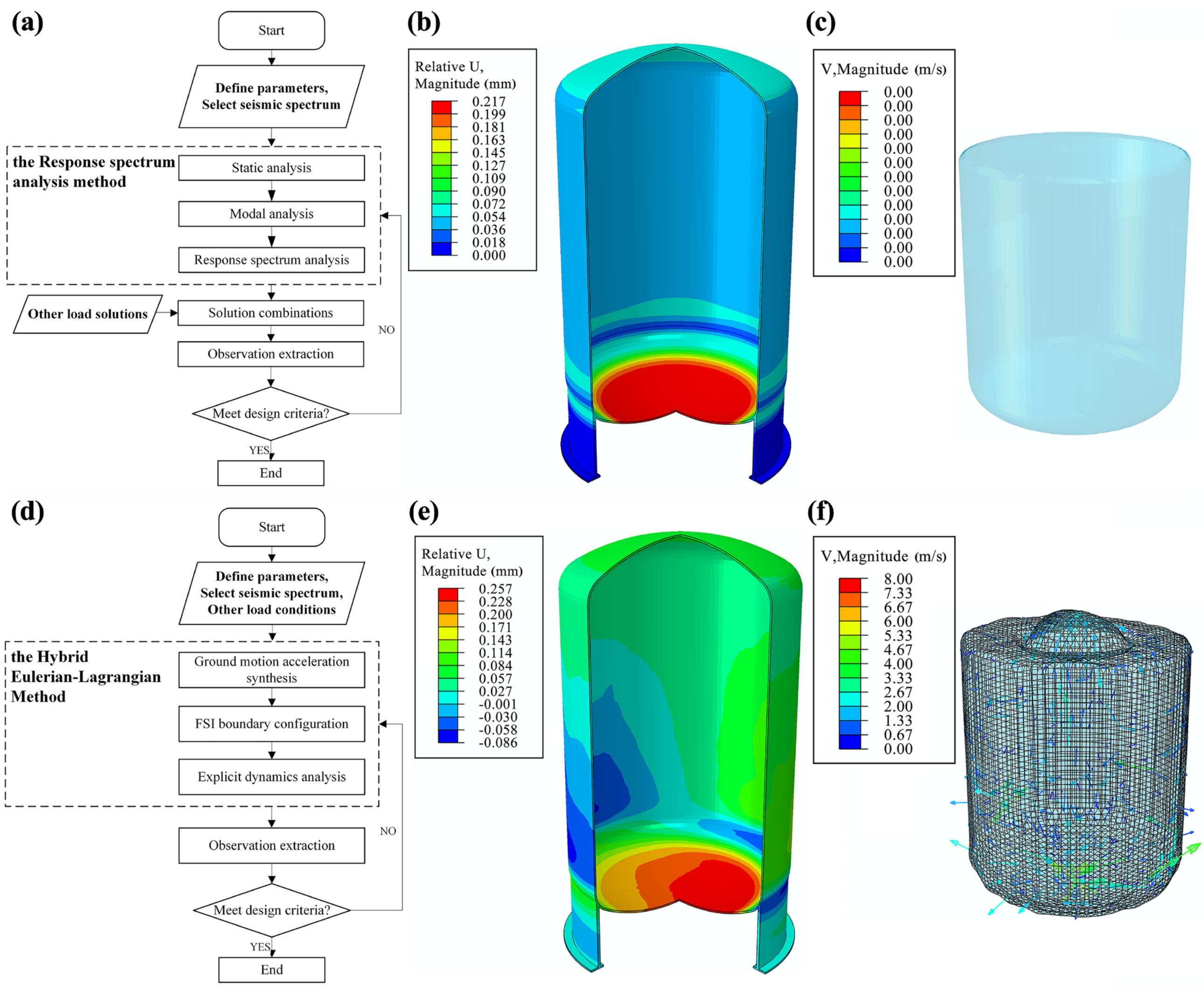

Fig. 14 (Color online) Comparison between the response-spectrum method and the HEL method for a tank with height 7 m, wall thickness 30 mm, and liquid-level L4. The top row **a**–**c** shows results from the response-spectrum method, and the bottom row **d**–**f** shows results from the HEL method. Subfigures correspond to: **a**, **d** Analysis flowchart; **b**, **e** Magnitude of relative displacement; **c**, **f** Magnitude of fluid velocity

displacement values, particularly in scenarios involving complex FSI. The HEL method, using a robust model for simulating fluid dynamics and structure interaction under seismic loading, demonstrates superiority in predicting liquid-containing structures' behavior under seismic influences. This method accounts for fluid nonlinear behavior, including sloshing and dynamic velocity, which are critical for reactor systems' integrity. This research highlights the limitations of applying the response-spectrum method in addressing the challenges associated with nuclear reactor systems; this method neither effectively considers varying liquid levels nor captures instantaneous dynamic responses essential for safety evaluation. The HEL method provides a comprehensive framework that enhances seismic impact prediction accuracy, advancing nuclear reactor safety. It fills gaps left by traditional analysis techniques, offering detailed assessment of potential risks in operating nuclear reactors in seismic zones. In conclusion, this study advocates for adopting sophisticated analytical methods such as the HEL method for the design and safety evaluation of nuclear facilities. Integrating such advanced simulation tools helps ensure critical infrastructure's structural integrity against seismic threats, ultimately leading to safer and more reliable energy production technologies.

Author contributions All authors contributed to the study conception and design. Material preparation, data collection and analysis were performed by Shi-Lin Chen, Qing-Xi Yang, and Qing-Zhou Yu. Software was developed by Shi-Lin Chen and Hao Xu. Visualization was performed by Hao Xu and Jian Chen. The first draft of the manuscript was written by Shi-Lin Chen. Supervision and funding acquisition were

provided by Qing-Xi Yang and Zhao-Xi Chen, and all authors commented on previous versions of the manuscript. All authors read and approved the final manuscript.

Data availability The data that support the findings of this study are openly available in Science Data Bank at https://cstr.cn/31253.11.sciencedb.j00186.00258 and https://www.doi.org/10.57760/sciencedb.j00186.00258.

Declarations

Conflict of interest The authors declare that they have no conflict of interest.

References

1. G. Locatelli, M. Mancini, N. Todeschini, Generation IV nuclear reactors: Current status and future prospects. Energy Policy **61**, 1503–1520 (2013). https://doi.org/10.1016/j.enpol.2013.06.101
2. Z. Zhang, Y. Dong, Q. Shi et al., 600-MWe high-temperature gas-cooled reactor nuclear power plant HTR-PM600. Nucl. Sci. Tech. **33**, 101 (2022). https://doi.org/10.1007/s41365-022-01089-9
3. M. Claessens, *ITER: The Giant Fusion Reactor* (Copernicus, Cham, 2023). https://doi.org/10.1007/978-3-031-37762-4
4. J. Zheng, J. Qin, K. Lu et al., Recent progress in Chinese fusion research based on superconducting tokamak configuration. Innovation **3**, 100269 (2022). https://doi.org/10.1016/j.xinn.2022.100269
5. K. Kowal, M. Torabi, Reliability and availability simulation for vessel cooling system of the high temperature engineering test reactor. Prog. Nucl. Energy **164**, 104888 (2023). https://doi.org/10.1016/j.pnucene.2023.104888
6. Q. Yu, S. Qiu, C. Wang et al., An experimental review of steam generator tube rupture accident in lead-cooled fast reactors: Thermal-hydraulic experiments classification and methods introduction. Prog. Nucl. Energy **160**, 104711 (2023). https://doi.org/10.1016/j.pnucene.2023.104711
7. Y. Liu, X. Meng, X. Wang et al., Transient analysis and optimization of passive residual heat removal heat exchanger in advanced nuclear power plant. Nucl. Sci. Tech. **33**, 106 (2022). https://doi.org/10.1007/s41365-022-01083-1
8. J. Lee, Evaluation of impacts of cooling tower design properties on the near-field environment. Nucl. Eng. Des. **326**, 65–78 (2018). https://doi.org/10.1016/j.nucengdes.2017.09.026
9. D.D. Andrea, Cryogenics in fusion: industrial approach of cryogenics applied to fusion plants. J. Fusion Energy **38**, 499–502 (2019). https://doi.org/10.1007/s10894-018-0196-8
10. A. Rydzy, G. Barone, A. Marini, The DTT secondary cooling water systems. Fusion Eng. Des. **158**, 111712 (2020). https://doi.org/10.1016/j.fusengdes.2020.111712
11. L. Berti, D. Aquaro, M. Raucci et al., Dust produced by plasma off normal event in the vacuum vessel: experimental analyses of the deposition inside the pressure suppression tank during a LOCA. Fusion Eng. Des. **190**, 113540 (2023). https://doi.org/10.1016/j.fusengdes.2023.113540
12. M. Tanaka, N. Suzuki, H. Kato et al., Estimation of tritium inventory in exhaust detritiation system for fusion test device in the initial tritium recovery operation. Fusion Eng. Des. **172**, 112808 (2021). https://doi.org/10.1016/j.fusengdes.2021.112808
13. J. Wu, Q. Yu, Q. Peng et al., Seismic responses of liquid storage tanks subjected to vertical excitation of near-fault earthquakes. Eng. Struct. **289**, 116284 (2023). https://doi.org/10.1016/j.engstruct.2023.116284
14. S.E.A. Hosseini, S. Beskhyroun, Fluid storage tanks: A review on dynamic behaviour modelling, seismic energy-dissipating devices, structural control, and structural health monitoring techniques. Structures **49**, 537–556 (2023). https://doi.org/10.1016/j.istruc.2023.01.146
15. R.J. Merino, E. Brunesi, R. Nascimbene, Probabilistic evaluation of earthquake-induced sloshing wave height in above-ground liquid storage tanks. Eng. Struct. **202**, 109870 (2020). https://doi.org/10.1016/j.engstruct.2019.109870
16. W. Jing, J. Feng, S. Wang et al., Failure probability of a liquid storage tank with three-dimensional base-isolation under earthquake action. Structures **58**, 105633 (2023). https://doi.org/10.1016/j.istruc.2023.105633
17. V. Ozsarac, E. Brunesi, R. Nascimbene, Earthquake-induced nonlinear sloshing response of above-ground steel tanks with damped or undamped floating roof. Soil Dyn. Earthq. Eng. **144**, 106673 (2021). https://doi.org/10.1016/j.soildyn.2021.106673
18. B.P. Ndemanou, A.N. Ndoukouo, J. Metsebo et al., Nonlinear energy sink response of a cylindrical storage tank under earthquake loads. Soil Dyn. Earthq. Eng. **179**, 108536 (2024). https://doi.org/10.1016/j.soildyn.2024.108536
19. R.A. Ibrahim, Liquid Sloshing Dynamics (Theory and Applications) (Cambridge University Press, 2005). https://doi.org/10.1017/CBO9780511536656
20. M. Takeda, Y. Ohkawa, Y. Akutsu, An evaluation method for seismic isolation effect in siting of a nuclear facility. Reliab. Eng. Syst. Saf. **62**, 241–249 (1998). https://doi.org/10.1016/S0951-8320(98)00023-4
21. Y. Cai, S. Wu, J. Yu, Structural analysis of the ITER VV lower port region. Plasma Sci. Technol. **9**, 492–495 (2007). https://doi.org/10.1088/1009-0630/9/4/24
22. X. Ni, S. Han, J. Ge et al., Seismic analysis of the vacuum vessel for CFETR. Fusion Sci. Technol. **78**, 352–359 (2022). https://doi.org/10.1080/15361055.2021.2021723
23. X. Peng, N. Mariani, A. Vostner et al., Structural integrity assessment for ITER lower VS coil feedthrough. Nucl. Fusion **61**, 036009 (2021). https://doi.org/10.1088/1741-4326/abd195
24. G. Mazzone, G. Sannazzaro, T. Schioler et al., Seismic design of the ITER main Tokamak components. Fusion Eng. Des. **86**, 1984–1988 (2011). https://doi.org/10.1016/j.fusengdes.2010.12.044
25. M. Khizer, J.W. Chen, G.W. Yang et al., Seismic and stress qualification of LMFR fuel rod and simple method for the determination of LBE added mass effect. Nucl. Sci. Tech. **31**, 5 (2020). https://doi.org/10.1007/s41365-019-0721-0
26. J.L. Almazán, F.A. Cerda, J.C. De la Llera et al., Linear isolation of stainless steel legged thin-walled tanks. Eng. Struct. **29**, 1596–1611 (2007). https://doi.org/10.1016/j.engstruct.2006.08.022
27. F.U.H. Mir, C.C. Yu, A.S. Whittaker, Experimental and numerical studies of seismic fluid-structure interaction in a base-supported cylindrical vessel. Earthquake Eng. Struct. Dyn. **50**, 1395–1413 (2021). https://doi.org/10.1002/eqe.3402
28. C. Bedon, C. Amadio, M. Fasan et al., Comparison of numerical strategies for historic elevated water tanks: modal analysis of a 50-year-old structure in Italy. Buildings **13**, 1414 (2023). https://doi.org/10.3390/buildings13061414
29. P. Hu, Z. Ma, T. Ma et al., Analysis of fluid structure interaction between fuel elements and the coolant in Xi'an Pulsed Reactor core under seismic conditions. Front. Energy Res. **11**, 1028079 (2023). https://doi.org/10.3389/fenrg.2023.1028079
30. W.C. Low, K.C. Ng, H.K. Ng, A SPH-lattice spring method for modelling Fluid Structure Interaction involving composite body and free surface. Comput. Part. Mech. **10**, 1587–1612 (2023). https://doi.org/10.1007/s40571-023-00576-z

31. Z. Dai, J. Xie, M. Jiang, A coupled peridynamics–smoothed particle hydrodynamics model for fracture analysis of fluid–structure interactions. Ocean Eng. **279**, 114582 (2023). https://doi.org/10.1016/j.oceaneng.2023.114582
32. A. Khayyer, H. Gotoh, Y. Shimizu et al., An improved Riemann SPH-Hamiltonian SPH coupled solver for hydroelastic fluid-structure interactions. Eng. Anal. Bound. Elem. **158**, 332–355 (2024). https://doi.org/10.1016/j.enganabound.2023.10.018
33. B. Blais, D. Vidal, F. Bertrand et al., Experimental methods in chemical engineering: Discrete Element Method-DEM. Can. J. Chem. Eng. **97**, 1964–1973 (2019). https://doi.org/10.1002/cjce.23501
34. J. Duriez, S. Bonelli, Precision and computational costs of level set-discrete element method (LS-DEM) with respect to DEM. Comput. Geotech. **134**, 104033 (2021). https://doi.org/10.1016/j.compgeo.2021.104033
35. Z.X. Shen, W.Q. Wang, C.Y. Xu et al., An innovative coupled common-node discrete element method-smoothed particle hydrodynamics model developed with LS-DYNA and its applications. China Ocean Eng. **38**, 467–482 (2024). https://doi.org/10.1007/s13344-024-0037-7
36. R. Verzicco, Immersed boundary methods: historical perspective and future outlook. Annu. Rev. Fluid Mech. **55**, 129–155 (2023). https://doi.org/10.1146/annurev-fluid-120720-022129
37. L. Wang, J. Young, F. Tian, An immersed boundary method for the thermo–fluid–structure interaction in rarefied gas flows. Phys. Fluids **36**, 013616 (2024). https://doi.org/10.1063/5.0181397
38. D. De Marinis, A. Mantegazza, A. Coclite et al., A fluid-structure interaction method for soft particle transport in curved microchannels. Comput. Meth. Appl. Mech. Eng. **418**, 116592 (2024). https://doi.org/10.1016/j.cma.2023.116592
39. I. Cheylan, T. Fringand, J. Jacob et al., Analysis of the immersed boundary method for turbulent fluid-structure interaction with Lattice Boltzmann method. J. Comput. Phys. **492**, 112418 (2023). https://doi.org/10.1016/j.jcp.2023.112418
40. D. Silva, R. Coelho, I. Pagonabarraga et al., Lattice Boltzmann simulation of deformable fluid-filled bodies: progress and perspectives. Soft Matter **20**, 2419–2441 (2024). https://doi.org/10.1039/d3sm01648j
41. D. Hui, G. Wang, M. Xia et al., Numerical study of interactions between Bingham fluids and flexible structures using the immersed boundary-lattice Boltzmann method. Phys. Fluids **36**, 023103 (2024). https://doi.org/10.1063/5.0188544
42. A.J. Oyejide, A.A. Awonusi, E.O. Ige, Fluid-structure interaction study of hemodynamics and its biomechanical influence on carotid artery atherosclerotic plaque deposits. Med. Eng. Phys. **117**, 103998 (2023). https://doi.org/10.1016/j.medengphy.2023.103998
43. M. Wichrowski, P. Krzyżanowski, L. Heltai et al., Exploiting high-contrast Stokes preconditioners to efficiently solve incompressible fluid–structure interaction problems. Int. J. Numer. Methods Eng. **124**, 5446–5470 (2023). https://doi.org/10.1002/nme.7350
44. D. Kalliontzis, V. Kotzamanis, Addressing geometric and material nonlinearities in fluid-structure interaction with the ALE-SSM framework. Eng. Struct. **295**, 116851 (2023). https://doi.org/10.1016/j.engstruct.2023.116851
45. Y. Cao, C. Liu, H. Tian et al., Mechanical behaviors of pipeline inspection gauge (pig) in launching process based on Coupled Eulerian-Lagrangian (CEL) method. Int. J. Press. Vessels Pip. **197**, 104622 (2022). https://doi.org/10.1016/j.ijpvp.2022.104622
46. F. Baharvand, S.M. Amiri, M.R. Shekari et al., A time domain nonlinear fluid–structure–soil interaction analysis of rectangular water storage tanks using coupled Eulerian-Lagrangian (CEL) formulation and direct method. J. Earthq. Eng. **28**, 1744–1768 (2024). https://doi.org/10.1080/13632469.2023.2252517
47. S. Sha, A.P. Dyson, G. Kefayati et al., Simulation of debris flow-barrier interaction using the smoothed particle hydrodynamics and coupled Eulerian Lagrangian methods. Finite Elem. Anal. Des. **214**, 103864 (2023). https://doi.org/10.1016/j.finel.2022.103864
48. P. Zakian, K. Bathe, Transient wave propagations with the Noh-Bathe scheme and the spectral element method. Comput. Struct. **254**, 106531 (2021). https://doi.org/10.1016/j.compstruc.2021.106531
49. P. Zakian, Stochastic spectral cell method for structural dynamics and wave propagations. Int. J. Numer. Methods Eng. **124**, 4769–4801 (2023). https://doi.org/10.1002/nme.7317
50. M.B. Hafeez, M. Krawczuk, A review: Applications of the spectral finite element method. Arch. Comput. Method Eng. **30**, 3453–3465 (2023). https://doi.org/10.1007/s11831-023-09911-2
51. A.K. Gupta, *Response spectrum method in seismic analysis and design of structures* (Routledge, 2017). https://doi.org/10.1201/9780203740781
52. R.N. Jazar, *Advanced Vibrations: Theory and Application* (Springer Nature, 2023). https://doi.org/10.1007/978-3-031-16356-2
53. P. Fajfar, Analysis in seismic provisions for buildings: past, present and future: The fifth Prof. Nicholas Ambraseys lecture. Bull. Earthq. Eng. **16**, 2567–2608 (2018). https://doi.org/10.1007/s10518-017-0290-8
54. R. Nascimbene, E. Fagà, M. Moratti, Seismic strengthening of elevated reinforced concrete tanks: analytical framework and validation techniques. Buildings **14**, 2254 (2024). https://doi.org/10.3390/buildings14072254
55. R. Nascimbene, G.A. Rassati, Seismic design and evaluation of elevated steel tanks supported by concentric braced frames. CivilEng. **5**, 521–536 (2024). https://doi.org/10.3390/civileng5020027
56. CEN, Eurocode 8: Design of structures for earthquake resistance – Part 1: General Rules, Seismic Actions and Rules for Buildings, EN 1998–1, Ed. 2004, CEN, European Committee for Standardization
57. ASCE, Minimum design loads and associated criteria for buildings and other structures, ASCE/SEI 7–16, Ed. 2017, ASCE, American Society of Civil Engineers
58. ICC, International Building Code, IBC 2018, Ed. 2018, ICC, International Code Council
59. O. Gazi, *Principles of Signals and Systems* (Springer Nature, 2022). https://doi.org/10.1007/978-3-031-17789-7
60. D. Zeidan, J. Merker, E.G. Da Silva et al., *Numerical Fluid Dynamics: Methods and Computations* (Springer Nature, 2022). https://doi.org/10.1007/978-981-16-9665-7
61. S. Kumar, *Fluid Mechanics (Vol. 2)* (Springer, 2023). https://doi.org/10.1007/978-3-030-99754-0
62. P. Zakian, A. Kaveh, Multi-objective seismic design optimization of structures: a review. Arch. Comput. Method Eng. **31**, 579–594 (2024). https://doi.org/10.1007/s11831-023-09992-z
63. Q. Zhu, Q. Han, J. Liu et al., High-accuracy finite element model updating a framed structure based on response surface method and partition modification. Aerospace **10**, 79 (2023). https://doi.org/10.3390/aerospace10010079
64. J. Ding, J. Zhou, W. Cai, An efficient variable selection-based Kriging model method for the reliability analysis of slopes with spatially variable soils. Reliab. Eng. Syst. Saf. **235**, 109234 (2023). https://doi.org/10.1016/j.ress.2023.109234
65. M. Benchikhoune, Methodology to be used to generate the seismic floor response spectra for ancillary buildings at ITER, ITER Document Management (IDM) system, ITER IDM: PN36V6 v3.0, (2015)
66. D. Combescure, Application of the FRS Simplified Methodology for the equipments close to the ground, ITER Document Management (IDM) system, ITER IDM: QZYDL3 v1.0, (2015)

67. J. Botija, J. Alonso, P. Fernández et al., Structural analysis of the JT-60SA cryostat vessel body. Fusion Eng. Des. **88**, 670–674 (2013). https://doi.org/10.1016/j.fusengdes.2013.02.120
68. IAEA, Seismic Design for Nuclear Installations, IAEA Safety Standards Series No. SSG-67, Ed. 2021, IAEA, International Atomic Energy Agency
69. AFCEN, Design and construction rules for mechanical components of nuclear installations, RCC-MR Ed. (2022), AFCEN, association francaise pour les regles de conception, de construction et de surveillance en exploitation des materiels des chaudieres electro-nuclealres
70. ASME, Boiler and Pressure Vessel Code Section VIII Division 1: Rules for Pressure Vessels, Ed. (2023), ASME, American Society of Mechanical Engineers
71. ASME, Boiler and Pressure Vessel Code Section VIII Division 2: Rules for Construction of Pressure Vessels, Alternative Rules, Ed. (2023), ASME, American Society of Mechanical Engineers
72. G. Rodolfo Saragoni, G.C. Hart, Simulation of artificial earthquakes. Earthq. Eng. Struct. Dyn. **2**, 249–267 (1973). https://doi.org/10.1002/eqe.4290020305